Theory and Design of Octave Tunable Filters with Lumped Tuning Elements

Akash Anand, *Student Member, IEEE,* Joshua Small, *Member, IEEE,* Dimitrios Peroulis, *Member, IEEE* and Xiaoguang Liu, *Member, IEEE*

***Abstract*—This paper presents octave-tunable resonators and filters with surface mounted lumped tuning elements. Detailed theoretical analysis and modeling in terms of tuning range and unloaded quality factor (Q_u) are presented in agreement with simulated and measured results. Based on the models, a systematic design method to maximize tuning ratio and optimize Q_u of the resonator is suggested. A resonator tuning from 0.5 GHz to 1.2 GHz with Q_u ranging from 84 to 206 is demonstrated using solid state varactors. A two-pole filter with tuning range of 0.5–1.1 GHz with a constant 3-dB fractional bandwidth (FBW) of 4 ± 0.1% and insertion loss of 1.67 dB at 1.1 GHz is demonstrated along with a three-pole filter with tuning range of 0.58–1.22 GHz with a constant 3-dB FBW of 4 ± 0.2% and insertion loss of 2.05 dB at 1.22 GHz. Measured input third order inter-modulation are better than 17 dBm over the frequency range for the two-pole filter.**

Keywords*—combline filter, combline resonator, evanescent-mode design, filter design, filters, full-wave simulation, measurement and modeling, modeling, tunable filters, tunable resonators, waveguide filters

I. Introduction

RECENTLY, there has been a growing interest in tunable RF/microwave filters. The driving parameters for these filters are low loss, wide tuning, low power consumption, small size, fast tuning, high power handling, and ease of fabrication at a low cost. Various demonstrated tunable filters excel in some parameters at the cost of sacrificing other parameters. For example, planer microstrip filters with lumped tuning components are easy to fabricate, but the unloaded quality factor (Q_u) suffers due to the low Q of the planer waveguides [1]–[3]. To achieve higher Q_u than planer structures, highly loaded 3-D evanescent-mode (EVA) resonators integrated with various types of tuning technologies have shown promising results [4]–[8]. For example, a tunable filter with piezoelectric actuator showed unloaded quality factor (Q_u) of 700–300 at 4.6–2.3 GHz [4]. Two EVA filters with RF-MEMS tuners, one with switched capacitor network and the other with silicon diaphragm, achieved Q_u of 500–300 at 5.58–4.07 GHz [5] and Q_u of 1000–300 at 6–24 GHz respectively [8]. While these technologies attain high Q_u, complexity arises in fabrication due to the precise assembly needed to either align the tuners with the EVA cavity's vertical gap (typically in μm) or insert the RF-MEMS switching network inside the cavity.

To avoid complicated fabrication and yet maintain high Q_u, 3-D cavities are integrated with commercially available surface mount tuning components as an alternative medium between low Q_u planer structures and high Q_u 3-D cavities. In [9], packaged RF-MEMS switches mounted on a substrate integrated waveguide (SIW) are used to get Q_u of 132–93 at 1.6–1.2 GHz. However the tuning range is limited to a few states. RF-MEMS capacitor banks mounted on a combline resonator resulted in Q_u of 1300–374 at 2.50–2.39 GHz with a limited tuning ratio (TR) of 1.05:1 [10], [11]. A surface ring gap combline resonator structure loaded with solid state varactors reports a Q_u of 160–40 with limited tuning range of 3.1–2.6 GHz [12], [13].

The authors of the current paper demonstrated a continuous octave tuning substrate-integrated combline resonator with Q_u of 86–206 and tuning range of 0.5–1.2 GHz using solid state varactors and Q_u of up to 240 at 6.6 GHz using RF-MEMS varactors [14]. It is the intention of this paper to further investigate this surface ring gap combline cavity. Compared to previous works [12]–[14], this paper presents an in depth theoretical analysis of the resonant frequency, TR, and Q_u. Effects of the parasitic capacitance of the surface ring gap and surface inductance are considered to show the compromise between tuning ratio (TR) and Q_u. A design method is suggested to maximize TR and optimize Q_u. This method demonstrates tunable resonators and filters with higher Q_u and tuning range than the state-of-the-art with similar technologies. A two-pole filter with tuning range of 0.5–1.1 GHz and measured insertion loss of 1.67 dB at 1.1 GHz is demonstrated. This two-pole filter maintains a constant 3-dB fractional bandwidth (FBW) of 4%. A three-pole filter with tuning range of 0.58–1.22 GHz with a constant 3-dB FBW of 4 ± 0.2% and measured insertion loss of 2.05 dB at 1.22 GHz is also demonstrated.

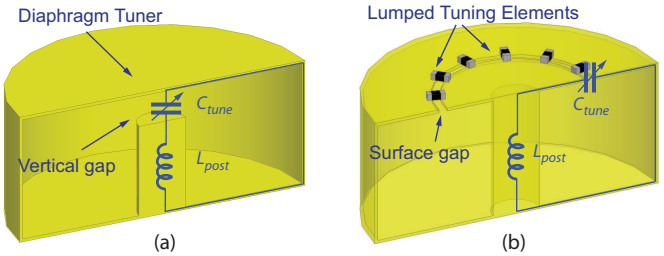

Fig. 1. (a) Vertical gap resonator and (b) surface ring gap resonator. Both have the same lumped equivalent circuit model.

II. Surface Ring Gap Combline Resonator

Figs. 1(a) and (b) schematically compares the cross-section of the typical vertical gap resonator with the cross section of

This paper is an expanded paper from the IEEE Int. Microwave Symposium held on June 2-7, 2013 in Seattle, WA.

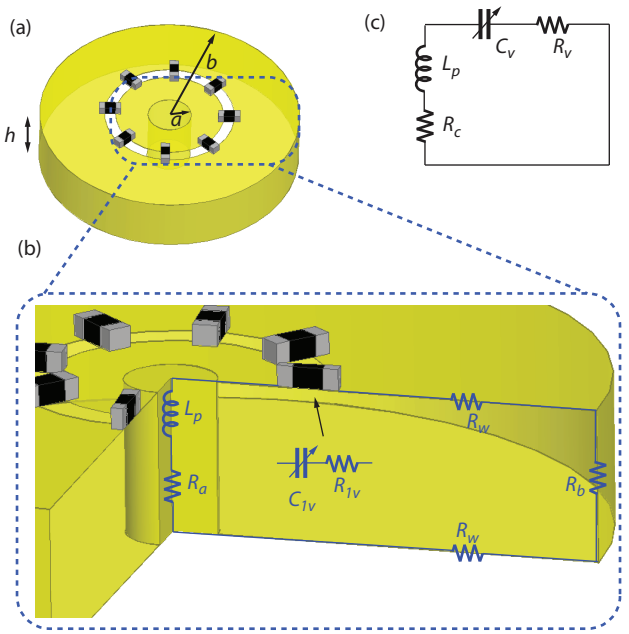

Fig. 2. (a) Cavity resonator with dimensions (b) cross sectional lumped model and (c) simplified LC resonator.

the proposed surface ring gap resonator. In the surface ring gap design, the center post is extended to short the bottom and top of the cavity and a ring gap is created on the surface to isolate the center post from the rest of the cavity's ceiling. To tune the resonant frequency, tuning elements are placed across the gap to vary the capacitance instead of having to change the physical gap. The figures show that the surface ring gap resonator still has the same lumped equivalent circuit model as the vertical gap resonator. The surface ring gap resonator in Fig. 1(b) resembles a shorted coaxial transmission line and is commonly referred as a combline resonator.

This design has several advantages compared to the vertical gap. First, the structure is not limited to a particular tuning technology but allows for various types of tuning components, such as RF-MEMS or solid state varactors. Second, precise assembly is not needed since the tuning components are surface mounted. This makes high-volume-manufacturing possible and the resonant frequency and tuning range independent of fabrication and assembly tolerance. Third, this structure is easily implemented on a low cost PCB, which can be integrated with other RF components. However, as shown later, this type of tuning may not yield Q_u in the order of $1,000$. Consequently, it is appropriate for applications that need Q_u in the order of 100–600 without the added complexity of vertically-aligned tuners.

III. Theoretical Analysis and Design

A. Resonant Frequency

Fig. 2(a) shows the dimensions of the resonator where h is the height of the cavity, a is the radius of the inner post, and b is the radius of the outer conductor. In Fig. 2(b), the resonator is approximated with lumped elements where L_p is the effective inductance of the cavity and capacitance C_{1v} in series with resistance R_{1v} models a varactor. The packaging and assembly, depending on the type of varactor (solid state, RF-MEMS, ect.), can introduce other parasitics. To keep the model generic, package parasitics are excluded and the varactor is assumed to operate well below its self resonance so the impedance resembles a series RC circuit. The conductors of the cavity, such as the inner post, outer wall, and the top and bottom walls, have resistances of R_a, R_b, and R_w respectively. A simplified model for the resonator is shown in Fig. 2(c) where C_v and R_v are the equivalent capacitance and equivalent resistance of all varactors and R_c is the sum of all other resistors.

For an L-C resonator, the angular resonant frequency ω is given as $1/\sqrt{LC}$. Thus, from Fig. 2(c), C_v and L_p are needed to find the resonant frequency of the resonator. The capacitance C_v is extracted from the equivalent impedance of the varactors Z_v, which is approximated as

$$Z_v = \frac{1}{N}\left(R_{1v} + \frac{1}{j\omega C_{1v}}\right) = R_v + \frac{1}{j\omega C_v}, \tag{1}$$

$$C_v = NC_{1v}, \tag{2}$$

$$R_v = \frac{R_{1v}}{N}, \tag{3}$$

where N is the number of varactors placed in parallel on the ring gap. Since the resonator resembles a shorted coaxial transmission line, L_p is extracted from the input impedance (Z_{in}) of a shorted transmission line

$$Z_{in} = jZ_o \tan(\beta h), \tag{4}$$

where

$$Z_o = \frac{377}{2\pi\sqrt{\epsilon_r}} \ln(b/a), \tag{5}$$

where Z_o is the characteristic impedance of the coaxial transmission line, ϵ_r is the dielectric constant of the material inside the cavity, and β is the phase constant. The above equations assume very low cavity losses, which is typically the case for the dimensions considered in this work. It has been shown that near resonance, the reactance of Z_{in} is inductive [15] and the effective inductance is approximated as

$$L_p = \frac{Z_o}{\omega} \tan\left(\frac{\omega h\sqrt{\epsilon_r}}{c}\right), \tag{6}$$

where c is speed of light. Assuming low losses, resonant frequency ω can be solved numerically in

$$\omega = \frac{1}{\sqrt{C_v L_p}}. \tag{7}$$

Eqn. (6) shows that L_p depends on ω, but the change is L_p is small (up to 3% for the cavity parameters and frequency range considered in this paper). Thus, neglecting the variation in L_p, the change in ω or tuning ratio TR, is determined by the tuning factor, $F_t = C_{1v\_ini}/C_{1v\_final}$, of the varactor

$$TR \approx \frac{1}{\sqrt{\frac{C_{1v\_final}}{C_{1v\_ini}}}} = \sqrt{F_t}. \tag{8}$$

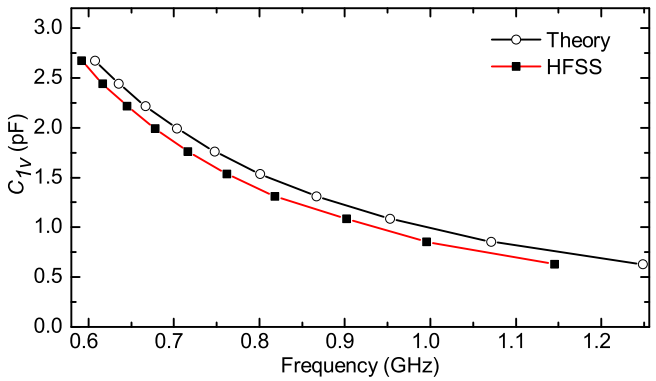

Fig. 3. Simulated and theoretical resonant frequency versus C_{1v} for the resonator. The difference between theory and simulation (up to 9%) is addressed in Fig. 10.

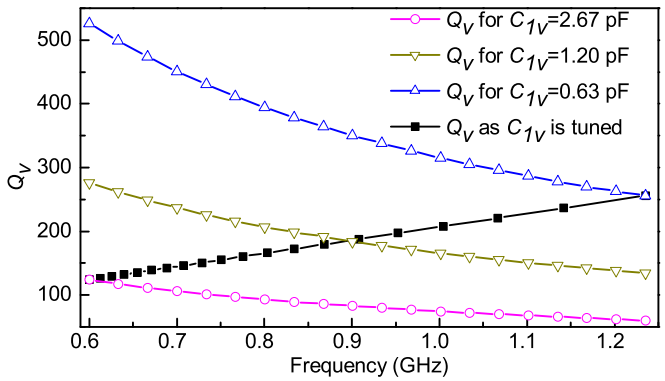

Fig. 4. Theoretical Q_v versus frequency for three fixed capacitances. As the capacitance is tuned, Q_v increases with frequency.

Ansys HFSS [16] is used to compare Eqn. (7) with full-wave simulations with the cavity parameters given in Table I. The surface gap radius r and surface gap width w is explained in section III-C. In Fig. 3, resonant frequencies from Eqn. (7) and HFSS simulations are plotted versus C_{1v}. Resonant frequencies from theory is between 3–9% higher primarily because Eqn. (7) does not include the effects of the gap capacitance and surface inductance (discussed later in section III-C and section III-D).

TABLE I. CAVITY DIMENSIONS USED IN HFSS SIMULATION

cavity parameter	value
h	5 mm
b	12 mm
a	0.512 mm
w	0.3 mm
r	3 mm
N	8
C_{1v}	0.63–2.67 pF
R_{1v}	0.8 Ω
ϵ_r	1
conductor	copper (0.5 mm)

B. Quality Factor

The resonator's Q_u is dependent on the quality factor of the varactors Q_v and the quality factor of the cavity Q_c. Since R_v is the resistance of the varactors, the series combination of R_v and C_v (see Fig. 2(c)) gives

$$Q_v = \left| \frac{imag\{Z_v\}}{real\{Z_v\}} \right| = \frac{1}{\omega C_v R_v}. \tag{9}$$

Substituting Eqn. (7) into Eqn. (9) and neglecting the variation in L_p gives Q_v ratio ($QR = Q_{v\_final}/Q_{v\_ini}$) as

$$QR \approx \frac{1}{\sqrt{\dfrac{C_{1v\_final}}{C_{1v\_ini}}}} = \sqrt{F_t}. \tag{10}$$

In Fig. 4, Q_v versus frequency for three different capacitances are plotted. For a fixed capacitance, Q_v decreases as frequency increases. However, as the varactor is tuned to a lower capacitance, larger F_t, Eqn. (10) and Eqn. (8) show that both Q_v and

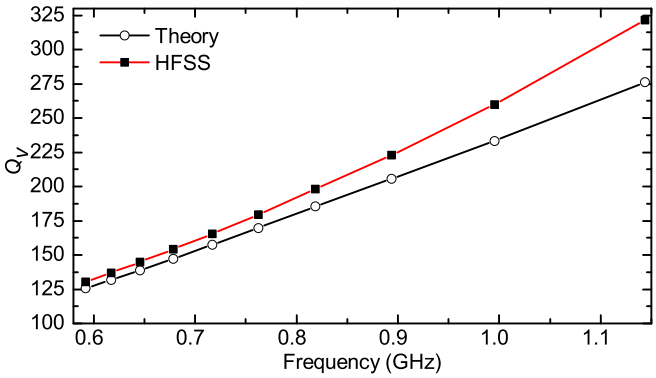

Fig. 5. Simulated and theoretical Q_v versus frequency for the resonator. The conductors of the cavity are simulated as perfect conductors to extract Q_v.

frequency will increase. Fig. 4 shows Q_v versus frequency as C_{1v} is tuned from 2.67 pF to 0.63 pF: Q_v increases from 124 at 0.6 GHz to 248 at 1.2 GHz. In Fig. 5, Eqn. (9) is compared to results from HFSS simulations. To extract Q_v from simulation, the conductors (post and walls of the cavity) are simulated as perfect conductors so that Q_v is approximately Q_u. The reason for higher Q_v in simulation is investigated in section III-C.

Since R_c is the resistance of the cavity conductors, the series combination of R_c with L_p (see Fig. 2(c)) gives

$$Q_c = \frac{\omega L_p}{R_c}, \tag{11}$$

which is essentially the quality factor of the cavity with lossless varactors. The sum of R_a, R_b, and R_w in Fig. 2(b) is R_c. From [17],

$$R_a + R_b = \frac{R_s}{2\pi}\left(\frac{h}{a} + \frac{h}{b}\right), \tag{12}$$

in which R_s is the surface resistance. Surface current density on the top and bottom of the cavity varies radially from the outer conductor to the inner post. Thus integrating in the radial direction gives

$$R_w = \frac{R_s}{2\pi} \ln\left(b/a\right). \tag{13}$$

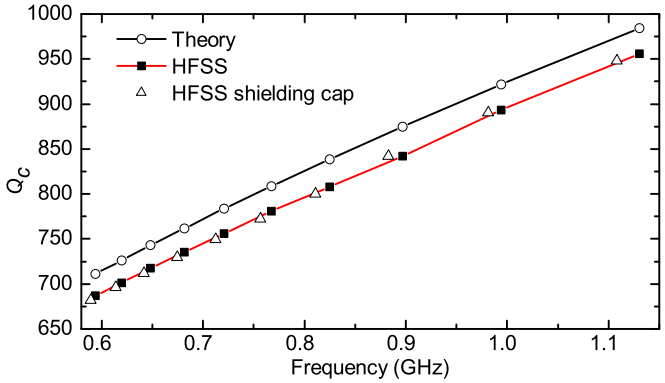

Fig. 6. Simulated and theoretical Q_c versus frequency for the resonator. In order to extract Q_c from HFSS, the resistance of the varactors are set to zero.

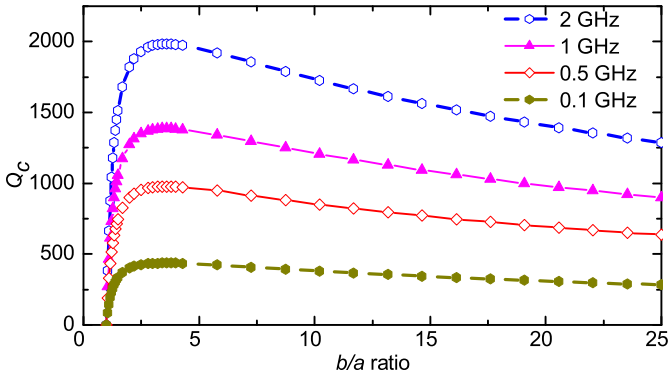

Fig. 7. Theoritical cavity Q_c with respect to b/a. Optimal Q_c is achieved at $b/a \approx 3.6$.

Summing Eqns. (12) and (13) gives R_c,

$$R_c = R_a + R_b + 2R_w = \frac{R_s}{2\pi}\left(\frac{h}{a} + \frac{h}{b} + 2\ln(b/a)\right) \quad (14)$$

Substitution Eqns. (6) and (14) into Eqn. (11) gives

$$Q_c = \frac{377\tan\left(\frac{\omega h\sqrt{\epsilon_r}}{c}\right)\ln(b/a)}{R_s\sqrt{\epsilon_r}\left(\frac{h}{a} + \frac{h}{b} + 2\ln(b/a)\right)}. \quad (15)$$

HFSS is used to compare Eqn. (15) with simulation with cavity parameters from Table I. In order to get Q_c only, R_{1v} in simulation is set to zero and C_{1v} is varied from 2.67 pF to 0.63 pF. Fig. 6 shows a plot of theoretical Q_c from Eqn. (15) compared to simulated Q_c. The simulated Q_c is about 3–4% lower than the theoretical one. Fig. 6 also shows that radiation from the ring gap has negligible effect by comparing simulation results from a resonator with a shielding cap covering the top. Note that the ring gap width w is about 100–200 times smaller than the wavelength range considered in simulation. Part of the 3–4% loss in simulation comes from the resistance associated with the ring gap which is considered in section III-C and Fig. 12.

The Q_c of a coaxial resonator is optimized when the b/a ratio is 3.6 [18]. This optimum ratio is again verified by plotting Eqn. (15) in Fig. 7. The outer radius and height of a copper air cavity are fixed to $b = 12$ mm and $h = 5$ mm while b/a is varied from 1 to 25 at four fixed frequencies: 0.1 GHz, 0.5 GHz, 1 GHz, and 2 GHz. The optimized b/a ratio is evident at all frequencies.

Using Eqns. (9) and (15) and the series L-C resonator model in Fig. 2(c), Q_u of the resonator is approximated as

$$\frac{1}{Q_u} = \frac{1}{Q_c} + \frac{1}{Q_v}. \quad (16)$$

The resonator's Q_u is simulated in HFSS with cavity parameters from Table I. Fig. 8 shows that simulation results are larger than theory because Q_v was larger in simulation previously (Fig. 5). In this case, Q_c is much larger than Q_v due to the relatively large R_{1v} (Fig. 6 and Fig. 5), so $Q_u \approx Q_v$. In Fig. 8,

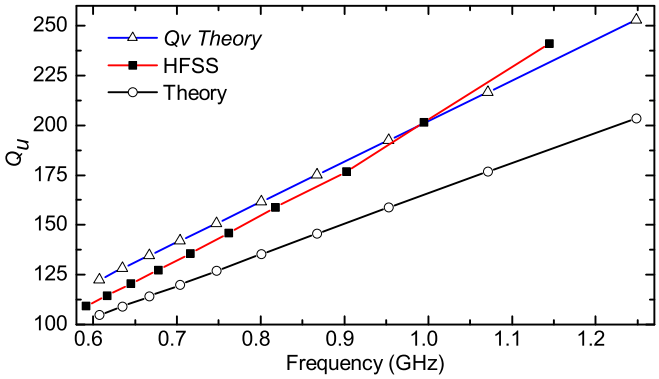

Fig. 8. Simulated and theoretical Q_u versus frequency for the resonator. Because Q_c is much larger than Q_v, $Q_v \approx Q_u$.

Q_u is initially limited by Q_v at lower frequencies (larger C_v) but starts to exceed Q_v at higher frequencies (smaller C_v). The limitations of $Q_u \approx Q_v$ is analyzed in more details in the next section.

C. Surface ring gap capacitance

In Fig. 3, the theoretical resonant frequency based on the lumped model in Fig. 2(c) was up to 9% higher than the simulated results. Part of this difference is due to the surface ring gap capacitance C_o. As shown in Fig. 9(a), this capacitance is dependent on the ring radius r, gap width w, depth of the gap d and the dielectric constant ϵ_r. Since C_o is in parallel with C_v, ω from Eqn. (7) is modified as

$$\omega = \frac{1}{\sqrt{(C_v + C_o)L}}, \quad (17)$$

where L is given by Eqn. (23). The value of C_o can be extracted from simulated ω at two different C_v values (C_{v1} and C_{v2}) for a fixed cavity structure from

$$\frac{\omega_1}{\omega_2} = \sqrt{\frac{(C_{v2} + C_o)}{(C_{v1} + C_o)}}, \quad (18)$$

where ω_1 is the resonant frequency for C_{v1} and ω_2 is the resonant frequency for C_{v2}. C_o is extracted for simulated data

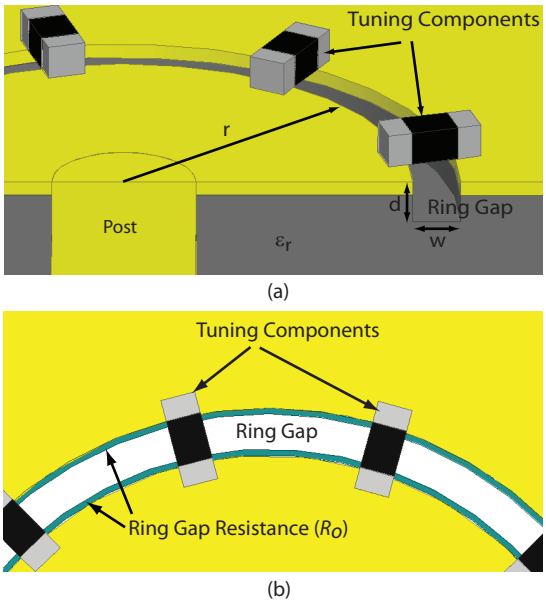

Fig. 9. Parasitic capacitance C_o exists in parallel with the tuning components (varactors). (a) C_o is dependent on the radius of the ring r, width of the gap w, depth of the gap d and the dielectric constant ϵ_r. (b) There is resistance R_o due to the wall plates (dark color region) around the surface ring gap.

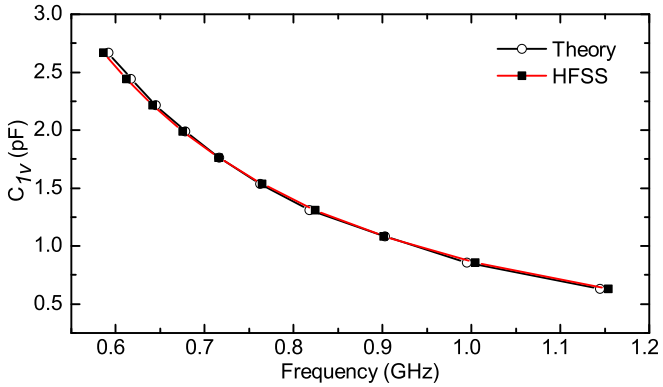

Fig. 10. Simulated and theoretical resonant frequency versus varactor capacitance when the effects of C_o is included. The difference in frequency is reduced to within 1%.

from Fig. 3 to be $C_o \approx 0.8$ pF. Compared to Fig. 3, when $C_o = 0.8$ pF is included in Eqn. (17), Fig. 10 shows the difference in resonant frequency is within 1% of simulation. The extraction of C_o here assumes that L is constant as C_v or w varies. The variation in L (Eqn. 23) and how to minimize the variation is considered in section III-D.

Since C_o is in parallel with C_v, the total electromagnetic energy will be distributed between C_v and C_o. Previously, if the conductors were lossless then $Q_u \approx Q_v$. However, if C_o is large enough, then a significant portion of the electromagnetic energy will be stored in C_o. Since the Q of C_o is expected to be higher than Q_v (resistance associated with C_o is small compared to R_{1v}), Q_u should exceed Q_v. This is however ac-

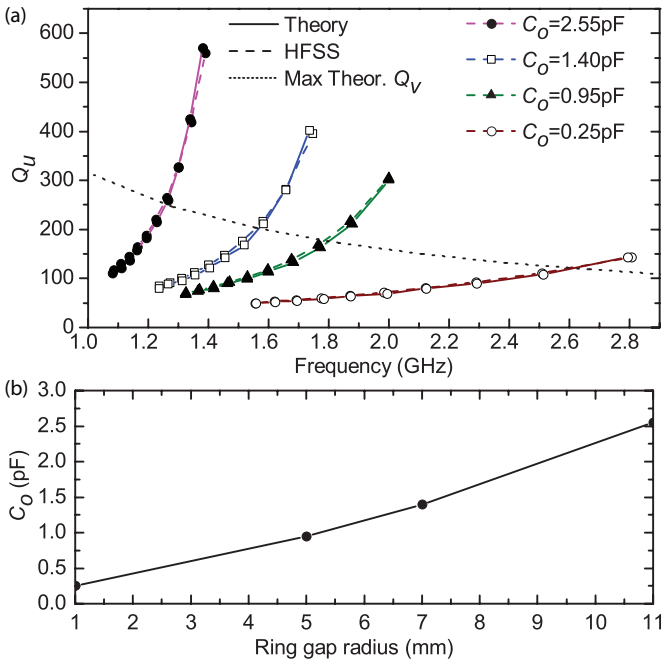

Fig. 11. (a)Theoretical Q_u (solid lines), simulated Q_u (dashed lines), and theoretical maximum Q_v (dotted line) versus frequency as C_o is changed. (b) Extracted C_o from simulation versus ring radius.

complished at the cost of reduced tuning range. The equivalent impedance, Z_{co} in parallel with Z_v, is given by

$$\frac{1}{Z_{eq}} = \frac{1}{Z_v} + \frac{1}{Z_{co}}, \tag{19}$$

where

$$Z_{co} = R_o + \frac{1}{j\omega C_o} \tag{20}$$

and R_o is the resistance associated with C_o shown in Fig 9(b) and is initially neglected ($R_o \approx 0$). Then Q of this impedance becomes

$$Q_{eq} = \left| \frac{imag\{Z_{eq}\}}{real\{Z_{eq}\}} \right|, \tag{21}$$

and Q_u from Eqn. (16) is modified as

$$\frac{1}{Q_u} = \frac{1}{Q_c} + \frac{1}{Q_{eq}}. \tag{22}$$

Note that if C_o is small and negligible, then Eqn. (22) reduces to Eqn. (16). Fig. 11(a) plots Eqn. (22) and HFSS simulation results showing the effect of C_o on Q_u and tuning range. C_{1v} is tuned from 2.67 pF to 0.63 pF. As C_o becomes larger, tuning range decreases and Q_u increases. Also plotted in the figure is Q_v at $C_v = 0.63$ pF (maximum Q_v). When C_o is larger, maximum Q_u for each curve is not limited by maximum theoretical Q_v (dotted line) and far exceeds Q_v. But as C_o decreases, maximum Q_u for each curve approaches maximum Q_v.

In the case of ideal varactors ($R_v = 0$) or when $C_o \gg C_v$, such as when no varactors are mounted in a static surface ring gap resonator [19], $Q_u = Q_c$ if $R_o = 0$. Fig. 9(b) shows

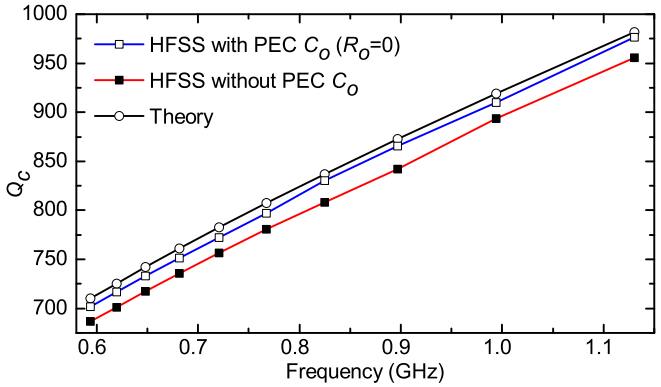

Fig. 12. Q_c is higher when the ring gap resistance is simulated with PEC ($R_o = 0$) compared to when ring gap resistance is simulated with copper ($R_0 \neq 0$). Simulation Q_c with $R_o = 0$ is within 1% of theoretical Q_c and simulation Q_c with $R_o \neq 0$ is within 3–4% of theoretical Q_c.

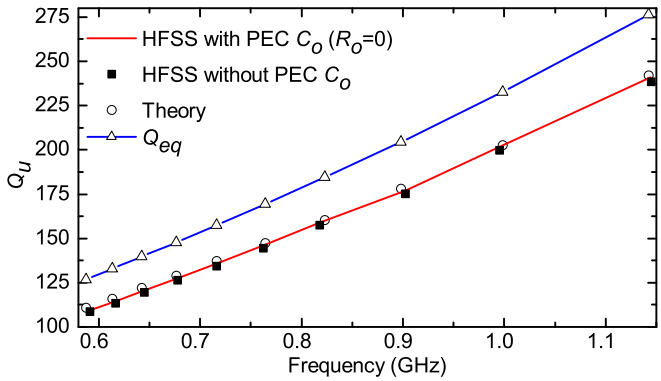

Fig. 13. Effects of R_o is negligible on Q_u for the cavity parameters considered in Table I since $R_v \gg R_o, R_c$. Additionally, theory and simulation Q_u are within 1% since the effects of C_o is included and Q_u is limited by Q_{eq}. Q_{eq} reduces to Q_v if $C_o = 0$.

that R_o depends on the two thin layers of metal wall (dark regions labeled as ring gap resistance in figure) that border the surface ring gap. These two thin walls are simulated in HFSS as a perfect conductors (PEC) or $R_o = 0$ while the rest of the cavity surface is still copper and $R_{1v} = 0$ with parameters from Table I. Fig. 12 compares Q_c of this PEC walls simulation with the previous case in Fig. 6 when all of the cavity surface was copper (no PEC or $R_o \neq 0$). As expected, Fig. 12 shows that Q_c with $R_o = 0$ is higher than Q_c with $R_o \neq 0$. Before, in Fig. 6, Q_c was 3–4% lower than theoretical Q_c (Eqn. 15), but with $R_o = 0$, simulation Q_c is within 1% of theoretical Q_c.

In Fig. 13, resistance of the varactors $R_{1v} = 0.8\ \Omega$ is included in HFSS simulation to compare Q_u when $R_o = 0$ and $R_o \neq 0$. Since R_v dominates both R_c and R_o, Fig. 13 shows that effects of R_o is negligible for the parameters in Table I. Thus the previous assumption of $R_o \approx 0$ made in Fig. 11 is valid. Also, compared previously to Fig. 8, theory and simulation are in better agreement, within 1%, now that the effects of C_o are included in theory. Moreover, this figure shows that Q_u is limited by Q_{eq}, which reduces to Q_v only if C_o is negligible.

In Fig. 11(a), the ring radius was changed to vary C_o. Fig. 11(b) shows that C_o is strongly dependent on r. C_o increases with increasing r (increasing circumference) since the surface area of the capacitance increases. Even though C_o has an air gap, the dielectric material of the cavity will partly change C_o due to fringing electromagnetic fields. Fig. 14 confirms this by showing the effects of various ϵ_r on resonant frequency and TR. The results in the figure are based on HFSS simulation with cavity parameters from Table I as C_{1v} ranges from 2.67 pF to 0.63 pF. Simulation shows that $TR = 1.93$ when $\epsilon_r = 1$ and $TR = 1.72$ when $\epsilon_r = 10$, a reduction of about 11% in TR. Based on Eqn. (18), $C_o \approx 0.8$ pF for $\epsilon_r = 1$, $C_o \approx 1.75$ pF for $\epsilon_r = 5$, and $C_o \approx 3$ pF for $\epsilon_r = 10$.

D. Surface inductance

The current that flows on the top surface from the inner post to the outer cavity wall results in a surface inductance

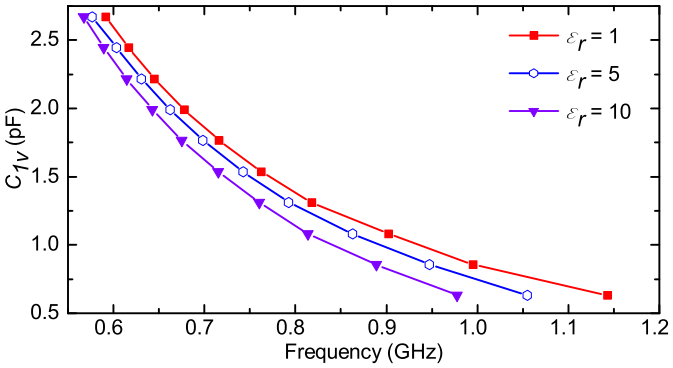

Fig. 14. Plot of frequency versus capacitance at various dielectric constants. As the dielectric constant increases, C_o increases and reduces TR.

L_o. This current flow depends on the ratio of Z_v and Z_{co}, and on N. If current flow is concentric, L_o will be minimal. The arrangement of the varactors can alter the current path, thus changing L_o.

(a) Consider the case of $Z_v \gg Z_{co}$. When N is large and the varactors are spatially distributed, current flows equally in all directions through the varactors and current flow is concentric. Fig. 15(a) illustrates this with $N = 8$. Fig. 15(b) shows current flow when N is small. Current is forced to flow through $N = 1$ varactor resulting in a longer current path. Thus L_o increases as N decreases, which is verified in Table II. In simulation, as N is varied, C_{1v} is also changed to keep C_v constant for different N values.

TABLE II. N VERSUS L_o

N	L_0 (nH)
1	0.68
2	0.3
4	0.25
8	0.2

(b) Consider the case of $Z_{co} \gg Z_v$. Since most of the current is distributed in the surface ring gap, current flow is

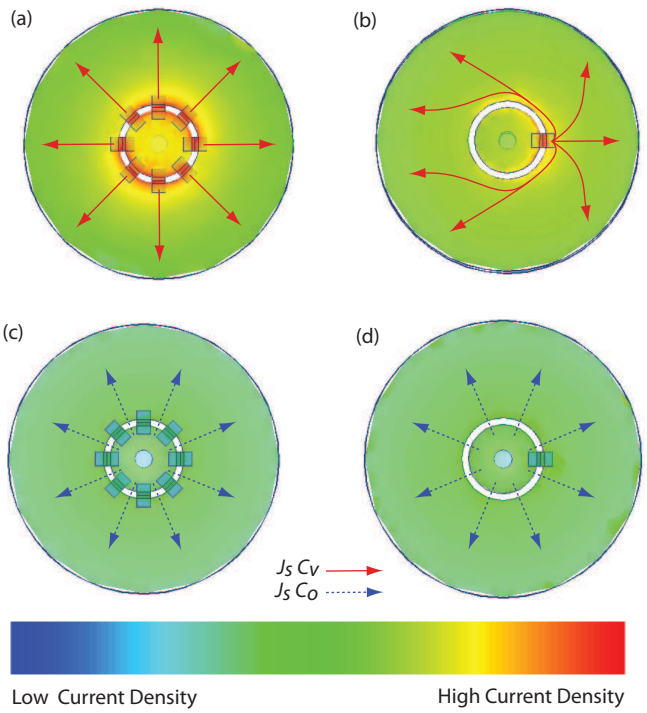

Fig. 15. HFSS simulation showing surface currents on the varactor loaded surface. (a) Current is equally distributed in 8 varactors and L_o is small. (b) Current flows through just one varactor which increases current path and L_o. (c) When C_o is dominant, current flows concentrically through C_o regardless of $N = 8$ or (d) $N = 1$.

concentric regardless of N. Figs. 15(c) and (d) show that current flow is concentric when $N = 8$ or when $N = 1$.

(c) When Z_v and Z_{co} are comparable, then current is distributed between the varactors and surface ring gap. If N is large and the varactors are equally spaced on the surface ring gap, current flow is concentric. For small N, current flow depends on ring radius r and F_t. As r gets larger, C_o gets larger and leads to a more concentric current flow, decreasing L_o. But also as r gets larger, the path of the current flow through the varactor gets longer, increasing L_o. Additionally, as F_t is tuned, C_v changes and the impedance ratio of C_o and C_v changes, making L_o vary with F_t. Thus, L_o is highly depended on r, Z_v/Z_{co} ratio, and F_t.

The surface inductance L_o is included in Eqn. (17) by replacing L with

$$L = L_p + L_o, \tag{23}$$

resulting in

$$\omega = \frac{1}{\sqrt{(C_v + C_o)(L_p + L_o)}}. \tag{24}$$

Though not discussed earlier, the effects of L_o is included in all the theoretical analysis and plots in section III-C. Even though L_o is dependent on various parameters, based on the above discussion, L_o is always minimal as long as N is sufficiently large. The effects of L_o is further reduced by increasing L_p. As mentioned previously and shown in Eqn. (6), L_p also varies slightly with ω. For $\epsilon_r = 1$, the variation in L_p is less than 0.4% and for $\epsilon_r = 10$, the variation in L_p is less than 3.5% over the frequency range with parameters from Table I.

E. Design Methodology

Based on the theoretical analysis, the compromise in Q_u and tuning range is highly dependent on C_o. With the aid of simulation software, appropriate C_o is designed by changing the surface ring gap dimensions or the dielectric constant (Fig. 11(b) and Fig. 14). For example, a resonator is designed for high Q_u, 160–40, but with a limited TR of 1.2 in [12]. This is analogous to the curve in Fig. 11 with $C_o = 1.6$ pF which has a TR of 1.22.

Alternatively, to design a resonator with maximum tuning range, C_o has to be minimized so that it is small relative to C_v. To maximize Q_c, b and h can be increased up to the size limitations and a can be set by the optimal $b/a = 3.6$ ratio. Then from (7) and (2), appropriate number of varactors N can be mounted to lower the frequency to the desired range, resulting in an optimized Q_u for a maximum TR design.

This design, however, may result in N that is too large. For example, a cavity with parameters from Table I, except with $a = 3.33$ mm for optimial b/a ratio, requires $N = 20$ varactors on the surface ring gap to tune from 0.6 GHz to 1.2 GHz. If fewer varactors are to be used, then the cavity dimensions may be changed to get the desired frequency range. The height and radius of the cavity are typically limited by the constraints on maximum device size. Varactors with larger capacitances are not recommended since the increase in capacitance comes at the cost of reduced Q_v, which directly limits Q_u. The reduction in tuning range and cost of high dielectric constant material restricts ϵ_r as a flexible parameter for design.

The optimum $b/a = 3.6$ ratio may need to be sacrificed to get the desired frequency range. From Eqns. (7) and (6), the resonant frequency depends on the b/a ratio. From Fig. 16, increasing b/a from the optimum ratio of 3.6 to 25 can decrease the frequency from f_o to $0.6f_o$. The previous example where $N = 20$ varactors were needed to tune from 0.6 GHz to 1.2 GHz can alternatively be designed by increasing the b/a ratio from 3.6 to 24. Fig. 17 shows a reduction of 5% to 7% in Q_u for $N = 8$ compared to $N = 20$.

IV. Experimental Validation

A. Resonator

A substrate-integrated-waveguide (SIW) combline resonator with solid state varactors as tuners is designed and fabricated to validate the theoretical derivations. Fig. 18(a) shows the designed resonator. In this design, metallic vias are inserted in a PCB substrate to create the outer wall of the cavity. The diameter ($\approx$ 1 mm) and the spacing of the vias ($<$ 3 mm) are designed with the recommendations given in [25] to keep losses minimal. Another center metallic via with radius of a shorts the bottom and top ceiling of the cavity. Fig. 18(b) shows the coplanar-waveguide (cpw) feed lines for this design with length F_l. Since solid state varactors are used, a structure

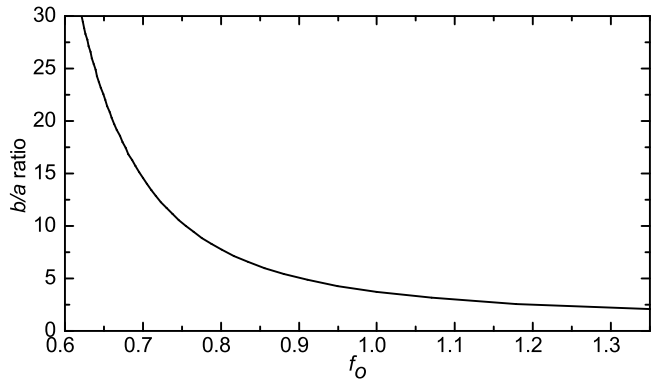

Fig. 16. Plot of b/a ratio versus normalized frequency f_o, where $f_o = 1$ is the resonant frequency for the optimum b/a ratio. The resonant frequency decreases by $0.6f_o$ as b/a is changed to 25.

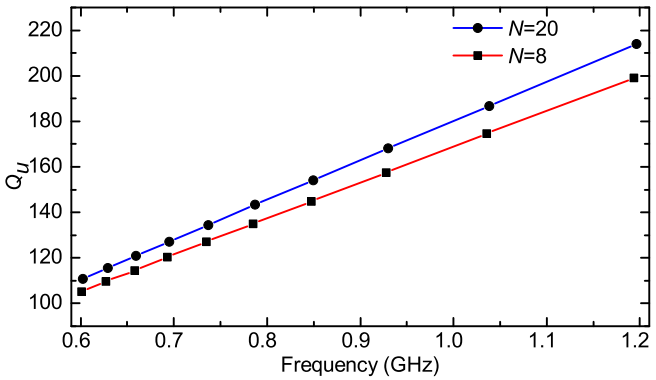

Fig. 17. A resonator can be designed with $N = 20$ with optimal b/a ratio equal to 3.6. Alternatively, the optimal b/a can be compromised ($b/a = 25$) to design a resonator with the same frequency range where fewer varactors are needed ($N = 8$) with reduced Q_u.

with two ring gaps is needed to create a bias point for the varactors. The two rings also allows for back-to-back varactor placement for improved linearity [20]. Since the additional ring is in series with the original ring, Eqn. 2 and Eqn.3 are modified to

$$C_v = \frac{N}{2} C_{1v}, \tag{25}$$

$$R_v = \frac{2}{N} R_{1v}. \tag{26}$$

In order to keep the same C_v and thus the same frequency range, N needs to be doubled for a two ring gap design compared to a one ring gap design.

The first part of the theoretical analysis was based on the lumped model presented in Fig. 2(c). In order for Eqn. (7) and Eqn. (16) to be valid, C_o and L_o had to be negligible. An SIW resonator is fabricated on a Rogers TMM3 substrate with the dimensions given in Table III. By choosing $N = 16$, the effects of C_o and L_o is minimized. Figs. 18(c) and (d) show the fabricated resonator and a close up of the arranged varactors with the isolated bias point for the varactors (not soldered on yet). Fig. 19 compares measured, HFSS, and theory. Q_u is plotted versus frequency as the varactors are biased from 0 V

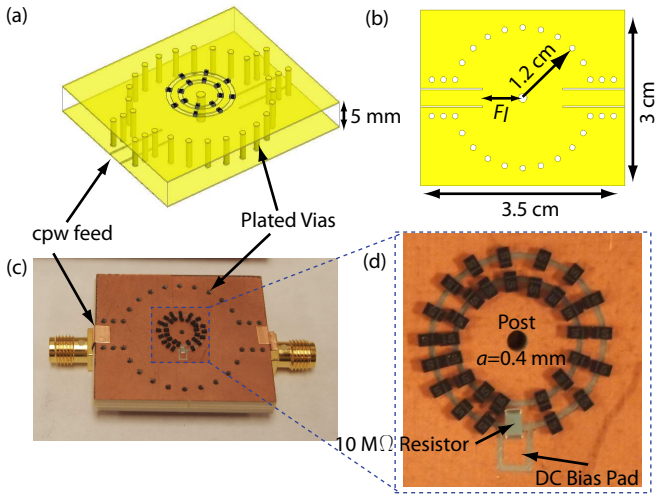

Fig. 18. (a) Designed resonator's top view and (b) bottom view showing cpw feed lines. (c) Rogers TMM3 substrate with vias and $N = 16$ Skyworks SMV1405 varactors. (d) Close up view of the two surface ring gaps showing the varactors (not soldered on yet) and the DC bias point.

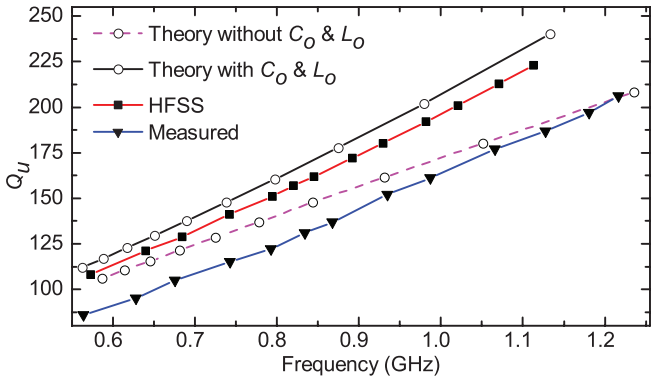

Fig. 19. Comparison of measured, simulated, theoretical (with and without C_o and L_o) Q_u versus frequency.

to 30 V. This figure validates that the simplified lumped model from Fig. 2(c) is reasonable in predicting ω and Q_u. As the fabricated C_o and L_o become even smaller, the lumped model should become closer to the measured results. Measured Q_u is lower due to losses in dielectric material (loss tangent is 0.002), fabrication, and assembly.

TABLE III. CAVITY DIMENSIONS USED IN FABRICATION

Cavity parameter	value
h	5 mm
b	12 mm
a	0.4 mm
w	0.3 mm
r	3 mm
varactor	Skyworks SMV1405
N	16
C_{1v}	0.63–2.67 pF
R_{1v}	0.8 Ω
substrate	Rogers TMM3
loss tangent	0.002
ϵ_r	3.37
conductor	copper (17.5 μm)

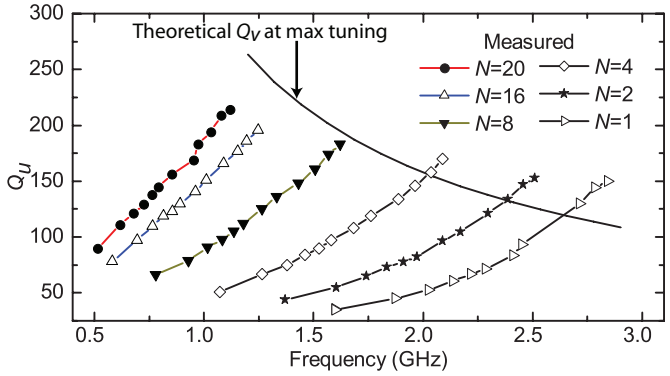

Fig. 20. Measured Q_u versus frequency for $N = 1$ to $N = 20$ along with maximum theoretical Q_v (solid line) at $C_v = 0.63$ pF. For larger N, $C_v \gg C_o$ and Q_u is limited by Q_v; as N decreases, C_o becomes comparable to C_v and Q_u exceeds Q_v

Part of the difference in measured versus theoretical ω and Q_u is caused by excluding C_o and L_o. Fig. 19 plots Q_u versus frequency including the effects of C_o and L_o, where $C_o = 0.6$ pF and $L_o = 0.3$ nH were extracted from measured data. The measured TR is about 2.1, simulated TR is about 1.94, and theoretical TR including the effects of C_o is 2.01. The slope of the curve with C_o and L_o is much closer to measured and simulation then the curve without C_o and L_o: Q_u increases as more electromagnetic energy gets distributed in C_o as C_v is tuned to a lower capacitance.

A resonator, with similar dimensions as Table III, is fabricated except with N ranging from 1 to 20. To compare the measured Q_u with Q_v, Fig. 20 includes a plot of theoretical Q_v at $F_t = 4.2$ (maximum Q_v). In the figure, Q_u is limited by Q_v when N is large, but exceeds Q_v for $N = 4$ or less– C_o has become significant compared to C_v. In fact, in the extreme case of $N = 1$, C_v is 0.315 pF, which is less than $C_o = 0.6$ pF. When the number of varactors N decreases, C_o/C_v ratio increases and TR decreases. Table IV summarizes the results of frequency range and TR. Table IV shows that the TR decreases from 2.17 when $N = 20$ to 1.78 when $N = 1$. Table IV also summarizes the results of Q_u and Q_u ratio at various N's. When $N = 20$ and thus C_v dominates, Eqn. (10) states that $\Delta Q_u = \sqrt{4.2} = 2.05$ which is close to the measured Q_u ratio of 2.38.

TABLE IV. SUMMARY OF MEASURED PERFORMANCE OF FABRICATED RESONATORS WITH VARYING N

N	freq (GHz)	TR	Q_u	QR
1	1.60–2.84	1.78	35–150	4.24
2	1.37–2.51	1.83	44–153	3.49
3	1.18–2.26	1.91	48–163	3.40
4	1.07–2.09	1.95	51–170	3.33
8	0.78–1.62	2.08	66–183	2.77
16	0.58–1.25	2.14	78–196	2.51
20	0.52–1.12	2.17	90–214	2.38

It should be noted that Q_u of the tunable resonator depends heavily on the tuner technology. In this case, solid state varactors have higher Q_v at lower frequencies. RF-MEMS tuners can be used to get high Q_u at higher frequencies. For example, the authors have demonstrated a surface ring gap resonator with Q_u of 240 at 6.6 GHz [14].

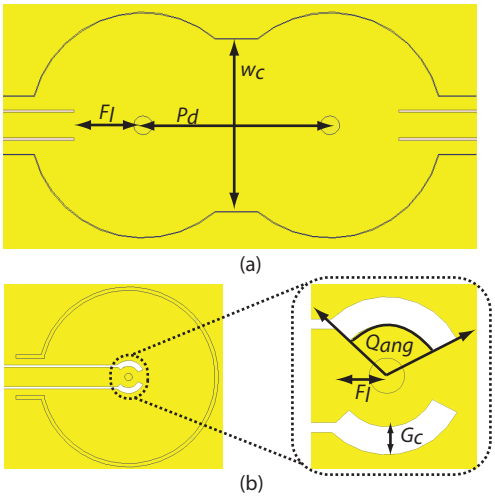

Fig. 21. (a) Two resonators with inter-resonator coupling K and weak external coupling. Both the width of the coupling iris w_c and post-to-post distance P_d can be changed to change K. (b) A one port resonator structure used to extract Q_e by varying the coupling angle Q_{ang} when the feed line F_l and coupling gap size G_c are constant.

B. Filter

To demonstrate the application of the resonator, a two-pole and a three-pole tunable filter are designed and fabricated with the resonator parameters from Table III. A similar procedure as outlined in [21] is used to get the external quality factor Q_e and inter-resonator coupling K from HFSS simulation. HFSS simulation is used to simulate various values of K by changing the width of the coupling iris w_c and the post distance P_d while the feed line F_l is kept far from the post (see Fig. 21(a)). Fig. 22(a) shows K versus P_d when $w_c = 1.6$ mm simulated around 1.1 GHz. A resonator with one port shown in Fig. 21(b) is used to simulated Q_e. As seen in the figure, another opening is created at the end of cpw feed lines with a coupling gap size G_c and coupling angle of Q_{ang}. Fig. 22(b) shows Q_e versus Q_{ang} when $G_c = 0.7$ mm and $F_l = 1.35$ cm is simulated around 1.1 GHz.

The required values of K_c and Q_e for a two-pole Butterworth filter response are

$$K_{1,2} = \frac{FBW}{\sqrt{g_1 g_2}} = 0.028, \tag{27}$$

$$Q_e = \frac{g_0 g_1}{FBW} = 35, \tag{28}$$

where $FBW = 4\%$, $g_0 = 1$, $g_1 = 1.4142$, and $g_2 = 1.4142$. Fig. 23(a) and (b) show the designed and fabricated two-pole filter with $w_c = 1.6$ cm, $Q_{ang} = 90$ degrees, and $F_l = 1.35$ mm in a $5 \times 3 \times 0.5$ cm^3 volume. The filter tunes from 0.5 GHz to 1.1 GHz with measured insertion loss from 4.46 to 1.67 dB and measured return loss from 8.3 to 27.8 dB (Fig. 23(c)). A $4 \pm 0.1\%$ FBW is maintained through out the tuning range. An Agilent PNA-X is used to measure input third-order inter-modulation intercept point (IIP3) with the two

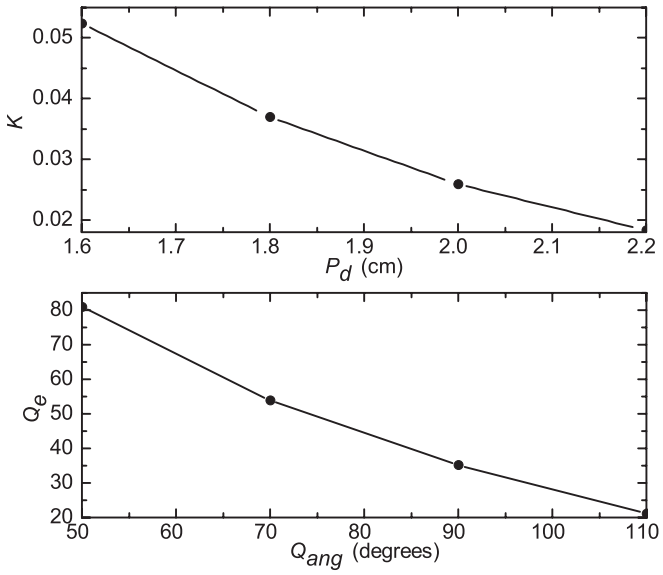

Fig. 22. Simulated design curves for (a) K versus post distance P_d and (b) Q_e versus coupling angle Q_{ang}

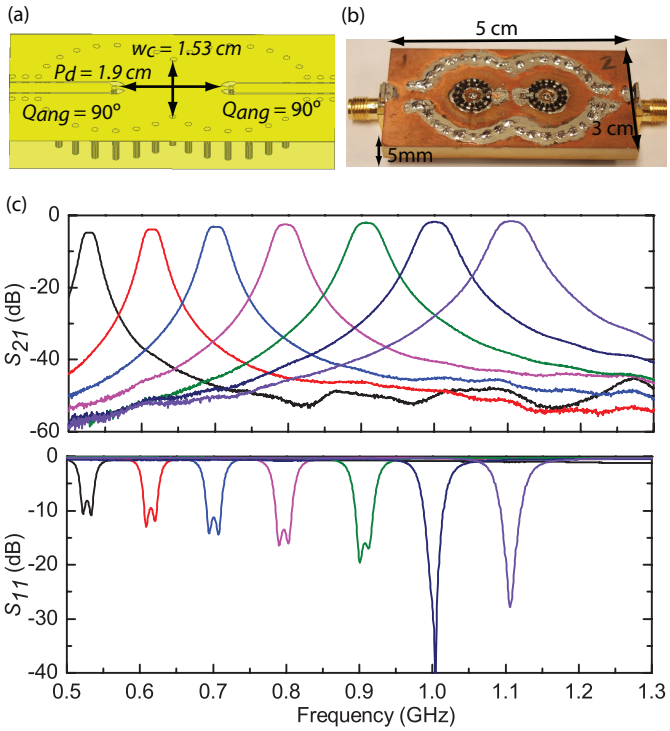

Fig. 23. (a) Designed and (b) fabricated octave tunable two-pole filter with measured (c) S_{21} and S_{11}.

tones separated by 100 kHz. The IIP3 ranged from 17 dBm to 30 dBm when the varactors were biased at 0–30 V. The required values of K_c and Q_e for a three-pole Butterworth filter response are

$$K_{1,2} = K_{2,3} = \frac{FBW}{\sqrt{g_1 g_2}} = 0.0283, \tag{29}$$

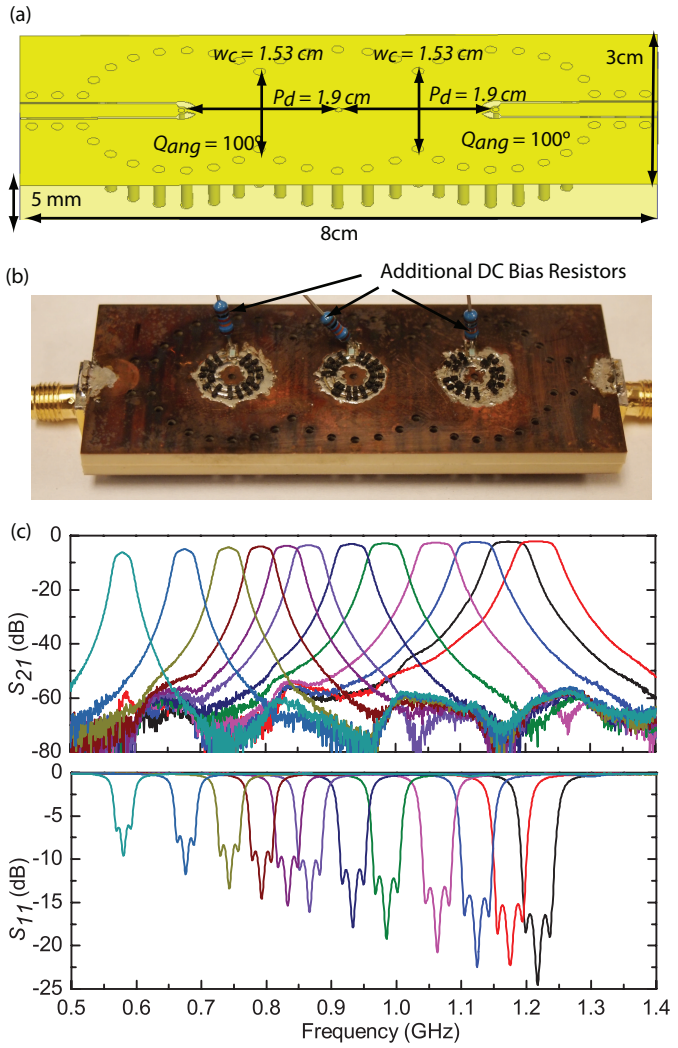

Fig. 24. (a) Designed and (b) fabricated octave tunable three-pole filter with measured (c) S_{21} and S_{11}.

$$Q_e = \frac{g_0 g_1}{FBW} = 25, \tag{30}$$

where $FBW = 4\%$, $g_0 = 1$, $g_1 = 1$, and $g_2 = 2$. Fig. 24(a) and (b) show the designed and fabricated three-pole filter with $w_c = 1.6$ cm, $Q_{ang} = 100$ degrees, and $F_l = 1.35$ mm in a $5 \times 3 \times 0.5$ cm^3 volume. For this filter, $N = 14$ is used for the resonators to get slightly higher frequency range of 0.58–1.22 GHz with a constant 3-dB FBW of $4 \pm 0.2\%$. Fig. 24(c) shows that the insertion loss varies from 6.2 dB at 0.58 GHz to 2.05 dB at 1.22 GHz.

Since both the two-pole filter and three-pole filter were designed at 1.1 GHz, the simulated K and Q_e values are best matched to the desired values at 1.1 GHz. As seen in Fig. 23(c) and Fig. 24(c), the return loss decreases as the filter is tuned to lower frequencies. In [26], a varactor is mounted on the cpw feed line to change Q_e and another varactor mounted between the two resonators to change K. Though [26] had a different resonator technology, the same concept of tunable

TABLE V. COMPARISON OF TUNABLE FILTERS

Ref.	Technology	F_t	TR	Freq. (GHz)	Q_u	Fabrication and Integration
[4]	Piezo	–	2.0	2.71–4.03	300–700	Complex
[5]	RF-MEMS	–	1.37	4.07–5.58	300–500	Complex
[6]	RF-MEMS	–	1.55	3.04–4.71	300–650	Complex
[13]	varactors	4	1.09	2.88–2.64	40–160	Simple
[9]	RF-MEMS	–	1.33	1.2–1.6	93–132	Simple
[22]	varactors	2.6	1.3	1.7–2.2	$\approx 110^*$	Simple
[23]	varactors	4.2	1.4	1.4–2.0	$\approx 50^*$	Simple
[24]	varactors	8.8	1.86	0.7–1.3	$\approx 150^*$	Simple
This	varactors	4.2	2.2	0.5–1.1	84–206	Simple

*Extracted at highest frequency

Q_e and K can be implemented in the presented filter design without added complexity. This allows Q_e and K to be tuned as the frequency response of the filter is tuned to improve return loss away from 1.1 GHz. However, adding more varactor will introduce more insertion loss.

Table V compares some of the recent tunable filters. As mentioned earlier and summarized in the table, the complexity of the presented surface ring gap resonator (and other planar varactor tuned filters) is reduced compared to some of the vertically aligned piezoelectric or RF-MEMS based filters. Moreover, to the best of authors' knowledge, the presented surface ring gap resonator exceeds the TR of all other solid state varactor based filters for a given varactor capacitance ratio (F_t): measured TR exceeds $\sqrt{F_t}$ (Eqn. (8)) for this work.

V. CONCLUSION

This paper presents the modeling and design of an octave tunable combline cavity filter using surface mount lumped tuning elements. Detailed theoretical analysis on the tuning range and Q_u of these resonators/filters are presented. A systematic design methodology is also proposed. To validate the theory and the design procedure, a tunable resonator with Q_u of 84–206 at 0.5–1.2 GHz, a two-pole tunable filter with tuning range of 0.5–1.1 GHz at a constant FBW of $4 \pm 0.1\%$ and measured insertion loss of 1.67 dB at 1.1 GHz, and a three-pole tunable filter with tuning range of 0.58–1.22 GHz at a constant FBW of $4 \pm 0.2\%$ and measured insertion loss of 2.05 dB at 1.22 GHz are demonstrated.

ACKNOWLEDGMENT

The authors would like to thank the National Defense Science and Engineering Graduate Program and the University of California, Davis Hellman Fellows Program for supporting this research.

REFERENCES

[1] M. A. El-Tanani and G. M. Rebeiz, "High-Performance 1.5-2.5-GHz RF-MEMS Tunable Filters for Wireless Applications," in *IEEE Trans. Microw. Theory Tech.*, vol. 58, no. 11, pp. 1629–1637, June 2010.

[2] C.-C. Cheng and G. M. Rebeiz, "High-Q 46-GHz suspended stripline RF MEMS tunable filter with bandwidth control," *IEEE Trans. Microw. Theory Techn.*, vol. 59, no. 10, pp. 24692476, Oct. 2011.

[3] S.-J. Park, K.-Y. Lee, and G. M. Rebeiz, "Low-loss 5.155.70-GHz RF MEMS switchable filter for wireless LAN applications" in *IEEE Trans. Microw. Theory Techn.*, vol. 54, no. 11, pp. 3931393, Nov. 2006.

[4] H. Joshi et al., "Highly loaded evanescent cavities for widely tunable high-Q filters," in *2007 IEEE MTT-S Int. Microw. Symp. Tech. Dig.*, Jun. 2007, pp. 2133−2136.

[5] S. J. Park et al., "High-Q RF-MEMS 4−6 GHz tunable evanescent-mode cavity filter," in *IEEE Trans. Microw. Theory Tech.*, vol. 58, no. 2, pp. 381−389, Feb. 2010.

[6] X. Liu et al., "High-Q tunable microwave cavity resonators and filters using SOI-based RF MEMS tuners," in *J. Microelectromech. Syst*, vol. 19, no. 4, pp. 774−784, Aug. 2010.

[7] X. Liu et al., "A 3.4–6.2 GHz Continuously Tunable Electrostatic MEMS Resonator with Quality Factor of 460–530," in *IEEE MTT-S Int. Microwave Symp. Digest*, June 2009, pp. 1149–1152.

[8] M. S. Arif and D. Peroulis, "A 6 to 24 GHz continuously tunable, micro-fabricated, high-Q cavity resonator with electrostatic MEMS actuation," in *IEEE MTT-S Int. Microwave Symp. Digest*, June 2012, pp. 1–3.

[9] V. Sekar, M. Armendariz, K. Entesari, "A 1.2-1.6-GHz Substrate-Integradeted-Waveguide RF MEMS Tunable Filter," in *IEEE Trans. Microw. Theory Tech.*, vol. 59, no. 4, pp. 866−876, Feb. 2011.

[10] S. Fouladi et al.,"Combline tunable bandpass filter using RF-MEMS switched capacitor bank," in *IEEE MTT-S Int. Microw. Symp. Dig.*, Jun. 2012.

[11] F. Huang et al.,"High-Q Tunable Dielectric Resonator Filters Using MEMS Technology," in *IEEE Trans. Microw. Theory Techn.*, vol. 59, no. 12, Dec. 2011.

[12] S. Sirci et al., "Varactor-Loaded Continuously Tunable SIW Resonator for Reconfigurable Filter Design," in *Proc. 41th. Eur. Microw. Conf.*, Oct. 2011, pp. 436-439.

[13] S. Sirci et al., "Analog Tuning of Compact Varactor-Loaded Combline Filters in Substrate Integrated Waveguide," in *Proc. 42th. Eur. Microw. Conf.*, Oct. 2012, pp. 257-260.

[14] A. Anand et al., "A Novel High-Q_u Octave-Tunable Resonator with Lumped Tuning Elements," in *IEEE MTT-S Int. Microwave Symp. Digest*, June 2013.

[15] G. F. Craven and R. F. Skedd, *Evanescent Mode Microwave Components*, Boston: Artech House, 1987.

[16] Ansoft Cooperation, *High Frequency Structure Simulator*. [Online]. Available: http://www.ansoft.com/products/hf/hfss/

[17] F. T. Ulaby, "Transmission lines" in *Fundamentals of Applied Electromagnetics*, media ed. New Jersey: Pearson Edu., Inc., 2004, ch. 4, pp. 41−42.

[18] P. Vizmuller, "Useful Formulas" in *RF Design Guide: Systems, Circuits and Equations*, Massachusetts: Artech House, Inc., 1995, ch. 2, pp. 238.

[19] J. Martinez et al., "Capacitively Loaded Resonator for Compact Substrate Integrated Waveguide Filters," in *Proc. 40th. Eur. Microw. Conf.*, Sept. 2010, pp. 192-195

[20] M. A. El-Tanani and G. M. Rebeiz, "Two-Pole Two-Zero Tunable Filter With Improved Linearity," in *IEEE Trans. Microw. Theory Tech.*, vol.57, no.4, pp. 830−839, April 2009.

[21] D. G. Swanson, "Narrow-band microwave filter design," in *Microwave Magazine, IEEE*, vol.8, issue 5, pp. 105−114, 2007.

[22] Xu-G. Wang,Y. Cho, and S. Yun, "A tunable combline bandpass filter loaded with series resonator", in *IEEE Trans. Microw. Theory Tech.*, vol. 60, no. 6, pp.1569-1576, June 2012.

[23] J. Long et al., "A tunable microstrip bandpass filter with two independently adjustable transmission zeros," in *IEEE Microw. Wireless Compon. Lett.*, vol. 21, no. 2, pp. 7476, Feb. 2011.

[24] A. R. Brown and G. M. Rebeiz, "A Varactor-Tuned RF Filter," in *IEEE Trans. Microw. Theory Tech.*, vol. 48, no. 7, pp. 1157−1160, July 2000

[25] K. Wu, D. Deslandes and Y. Cassivi, "The Substrate Integrated Circuits - A New Concept for High-Frequency Electronics and Optoelectronics," in *Telecommunications in Modern Satellite, Cable and Broadcasting Service*, vol. 1, Oct. 2003

[26] H. Joshi et al., "High-Q Fully Reconfigurable Tunable Bandpass Filter,"

in *IEEE Trans. Microw. Theory Tech.*, vol. 57, no. 12, pp. 3525–3533, Dec. 2009.

Akash Anand (S'12) received the B.S. degree in electrical engineering from University of California, Davis in 2009. He is currently working towards his Ph.D. degree at University of California, Davis. His research interest includes RF/microwave tunable filters, RF and analog IC design, and reconfigurable RF systems.

Joshua Small (S'11–M'12) received the Bachelor's degree in electrical engineering from Morgan State University, Baltimore, MD in 2005 and the Ph.D. degree from Purdue University, West Lafayette, IN in 2012.

He is currently a postdoctoral research engineer with the Department of Electrical and Computer Engineering at University of California Davis. Dr. Small's research interests includes investigating novel high-Q microstructures for reconfigurable radio front ends.

Dr. Xiaoguang "Leo" Liu (S'07–M'10) received his B.S. degree from Zhejiang University, China in 2004 and his Ph.D. degree from Purdue University in 2010. He is currently an assistant professor in the Department of Electrical and Computer Engineering at the University of California, Davis. His research interests include RF-MEMS and other reconfigurable RF/microwave components, software defined radios, and terahertz components and systems. He has published over 30 papers in peer-reviewed journals and conferences. As a student, he received the graduate research fellowship from IEEE Antenna and Propagation Society in 2009. He was selected as a UC Davis Hellman Fellow in the 2013-2014 academic year.